

# Elucidating morphological effects in membrane mineral fouling using real-time particle imaging and impedance spectroscopy

Chidiebere S. Nnebuo, Denise Hambsch, Oded Nir\*✉

*Department of Desalination and Water Treatment, Zuckerberg Institute for Water Research, Jacob Blaustein Institutes for Desert Research, Ben-Gurion University of the Negev, Sede-Boqer Campus 84990, Israel*

\*Corresponding author ✉[odni@bgu.ac.il](mailto:odni@bgu.ac.il)

## Abstract

Mineral fouling is a major hindrance to high recovery effluent nanofiltration, with calcium phosphate (Ca-P) and calcium carbonate ( $\text{CaCO}_3$ ) the most prevalent mineral foulants. In this study, we used a novel combination of real-time in-line microscopy, electrical impedance spectroscopy (EIS), post SEM analysis, and filtration metrics (water flux and rejection) to study mineral fouling mechanisms of Ca-P and  $\text{CaCO}_3$  salts in synthetic effluent nanofiltration. We used nanofiltration (NF) polyelectrolyte multilayer (PEM) membranes, prepared by static layer-by-layer (LbL) coating of a cationic polymer - polydiallyl dimethylammonium chloride, and anionic polymer - poly styrenesulfonate (six bi-layer) on a polyethersulfone (PES) ultrafiltration (UF) membrane. Increasing permeate recovery over filtration time was simulated through additions of  $\text{CaCl}_2$  with  $\text{NaHCO}_3$  or  $\text{NaH}_2\text{PO}_4/\text{Na}_2\text{HPO}_4$ . Using the novel combination of methods, we delineated the mechanisms governing fouling development with time for both  $\text{CaCO}_3$  and Ca-P. For  $\text{CaCO}_3$ , a transition from heterogeneous precipitation on the membrane surface (scaling) to particulate fouling due to bulk precipitation was identified. For Ca-P, a transition from fouling by amorphous particles to fouling by crystalline particles was identified; and this phase-change was captured in real-time images using an in-line microscope. We also found that for similar precipitation potentials measured by weight, Ca-P fouling was more detrimental to water flux (86%

decrease) compared to  $\text{CaCO}_3$  (20% decrease) due to the voluminous amorphous phase. We established in-line microscopy as a new useful method to study mineral fouling, as it gives invaluable information on the suspended particles in real-time. Combining it with EIS gives complementary information on mineral accumulation on the membrane surface. Insight from this study and further use of these methods can guide future strategies towards higher effluent recovery by membrane filtration.

**Keywords:** membrane scaling; effluent nanofiltration; calcium phosphate; calcium carbonate; in-line microscopy;

## 1. Introduction

Recycling of wastewater has a vital role in tackling global water scarcity, as the effluent is a largely untapped water resource with stable supply year-round (Almuktar et al., 2018; Farhadkhani et al., 2018; Friedler, 2001; Oron et al., 2008; Tran et al., 2016). However, wastewater effluent contains various persistent contaminants that pose a risk to public health and the environment (Garcia and Pargament, 2015; Grandclément et al., 2017; Murgolo et al., 2019; Wintgens et al., 2005). These contaminants may include excess phosphorus, emerging/trace organic contaminants (ECs/TrOCs) such as pharmaceuticals and personal care products (PPCPs), endocrine disrupting compounds (EDCs), trace elements (Grandclément et al., 2017), steroid hormones, surfactants, industrial chemicals (Luo et al., 2014), pesticides and inorganic salts (Wintgens et al., 2005). Since conventional water treatment plants cannot properly remove these contaminants (Luo et al., 2014; Nghiem and Fujioka, 2016), it is widely acknowledged today that further treatment is needed for sustainable reuse and safe discharge of tertiary effluent.

To attain various water quality requirements necessary for different wastewater recycling uses, membrane processes like reverse osmosis (RO) and nanofiltration (NF) have emerged

as the best available technology (Bunani et al., 2013; Lee and Lee, 2005; Mohammad et al., 2015; Nghiem and Fujioka, 2016; Wintgens et al., 2005). RO membranes reject most dissolved molecules and thus can bring the tertiary effluent to drinking-water quality level, enabling potable use, either directly (e.g., Singapore) or indirectly through aquifer recharge (e.g., California). NF membranes remove all microorganisms and most of the organic micropollutants and dissolved phosphorus (depending on membrane type). Therefore NF-treated effluent can be exploited in non-potable uses such as irrigation, rehabilitation of water supply to natural water bodies (Garcia and Pargament, 2015; Oron et al., 2008), and creating artificial water bodies for recreational activities or ornamentation. While RO is the standard for potable reuse of tertiary effluent, using NF membranes offer some leverage over RO membranes in non-potable reuse; including lower operating pressure, tuneable selective removal of salts/solutes, and the availability of more robust membrane materials (Mohammad et al., 2015; Nir et al., 2018; Schäfer et al., 1998). Therefore, in light of the global increase in wastewater reuse and stricter effluent discharge regulations, the application of RO and NF processes for wastewater treatment is expected to increase.

A key drawback to membrane processes application to wastewater recycling is the high cost of retentate stream management (Chang et al., 2009; Greenlee et al., 2010; Kappel et al., 2014; Voutchkov, 2011). A retentate stream of RO/NF applied to wastewater, typically 10-30% of the feed water volume, contains the various contaminants removed from the effluent at higher concentrations. Therefore, there is a need to minimize the retentate volume by operating at a higher permeate recovery ratio to achieve cost-effective and sustainable RO/NF processes. However, the recovery ratio in effluent NF/RO is currently limited by chemical fouling, mainly caused by the precipitation of calcium phosphate (Ca-P) and calcium carbonate (CaCO<sub>3</sub>) minerals (Greenberg et al., 2005), reaching supersaturation when concentrated in the retentate. Commonly used strategies for scaling control can be grouped

into (a.) scalants removal by pre-treatment of feedwater (b.) scaling inhibitors use (c.) process-based strategies (Tong et al., 2019). While,  $\text{CaCO}_3$  scaling can be effectively controlled by adjusting the pH and use of antiscalants (Chaussemier et al., 2015), Ca-P minerals could precipitate at  $\text{pH} < 6$ , and no effective antiscalants are currently available for controlling Ca-P fouling (Antony et al., 2011; Greenberg et al., 2005; Mangal et al., 2021; Steiner et al., 2010). Developing novel solutions calls for a better understanding of the chemical fouling mechanisms of these scalants during effluent filtration.

Mineral fouling occurs when sparingly soluble salts are rejected by the membrane, and consequently, their concentration increases in the retentate until it reaches a supersaturation level that is sufficiently high to induce crystallization (Tong et al., 2019). Supersaturation is further increased near the membrane surface due to concentration polarization (CP) (Antony et al., 2011; Lee and Lee, 2005, 2000; Van De Lisdonk et al., 2000). The evolution and dynamics of mineral scaling are influenced by several factors including, pH (Klepetsanis and Koutsoukos, 1989), flow velocity (Lee and Lee, 2000), Ca/P ratio, presence of other salts ( $\text{Mg}^{2+}$  for  $\text{CaCO}_3$ ) (Chen et al., 2006; Roques and Girou, 1974), operating pressure (Lee and Lee, 2000), physicochemical membrane surface properties (Rathinam et al., 2018), and ion rejection rate (Kaganovich et al., 2019). Mineral fouling can progress through homogeneous-like precipitation/crystallization in the bulk or heterogeneous surface crystallization (Gilon and Hasson, 1987; Lee and Lee, 2005). Mineral particles formed in the bulk may deposit on the membrane surface to form a cake layer, whereas, in surface crystallization, the scaling layer grows laterally on the membrane surface.. Tzotzi et al. (2007) identified heterogeneous-surface crystallization as the primary mechanism for  $\text{CaCO}_3$  NF scaling of tap water, while Xu et al. (2010) reported colloidal fouling as the primary mechanism of Ca-P salt in nanofiltration of effluent. While both routes can hinder filtration performances, removing a scaling is typically more challenging or even not practical (Antony et al., 2011).

Although mineral fouling is affected by processes occurring both in the retentate and on the membrane surface, there are little or no reports on parallel measurements of these processes. Such data can, for instance, delineate between scaling and particulate fouling. Moreover, little or no attention was given to the role of mineral morphology in effluent nanofiltration. Elucidating morphological effects can be challenging, especially for Ca-P minerals, including multiple possible phases of different morphologies. We used a novel combination of in-line real-time particle microscopy and in-situ electrochemical impedance spectroscopy (EIS) to address these knowledge gaps. We conducted nanofiltration experiments, where we gradually added scaling ions to simulate the increase in supersaturation and the accumulation of crystal mass associated with mineral fouling. The data collected from these novel systems, together with water and salt permeation data and post-filtration electron microscopy, elucidated the underlying micro-scale phenomena and the mechanistic differences between the two mineral types studied here. These differences affected the membrane performance and pointed toward different mitigation methods for Ca-P and  $\text{CaCO}_3$  mineral fouling.

## **2. Materials and method**

### **2.1. Materials**

The following chemicals were obtained from Merck company the U.S.A.;  $\text{MgSO}_4 \cdot 7\text{H}_2\text{O}$ ; KCl;  $\text{CaCl}_2 \cdot 2\text{H}_2\text{O}$ ; NaCl;  $\text{Na}_2\text{HPO}_4 \cdot 2\text{H}_2\text{O}$ ;  $\text{NaH}_2\text{PO}_4 \cdot \text{H}_2\text{O}$  while  $\text{NaHCO}_3$  and Nitric acid (70%) were obtained from Bio-lab company Israel; AnalaR BDH Laboratory Supplies Israel supplied  $\text{Na}_2\text{HPO}_4$ ; Sigma Aldrich supplied  $\text{NaH}_2\text{PO}_4$ . All chemicals were of analytical grade.  $\text{Na}_2\text{HPO}_4$  and  $\text{NaH}_2\text{PO}_4$  were used to make a phosphate buffer of 0.1M (at a pH 7) in the ratio of 0.65:0.35. The phosphate buffer was used throughout the experiments for membrane integrity P rejection tests. Polyethersulfone (PES) ultrafiltration (UF) membranes

with molecular weight cut-off (MWCO) of 20kDa was obtained from Sterlitech U.S.A; Polydiallyldimethylammonium chloride (PDADMAC) MWCO = 400 – 500 kDa and Poly(styrenesulfonate) (PSS) MWCO = 1000 kDa were also purchased from Sigma Aldrich while deionized (DI) water  $< 2 \mu\text{S}/\text{cm}$  was used during the experiments. The procedure for layer-by-layer coating of PES membrane into an NF polyelectrolyte multilayer membrane (PEMM) is available at supporting information (SI) S1.0.

## **2.2. V19 particle view microscope**

V19 Particle view<sup>TM</sup> Mettler Toledo AG (U.S.A) is a probe-based video microscope and an in-line in-situ tool for real-time monitoring of the particle development in the feed during filtration. Particle V19 (iC PVM) measurement is a particle vision measurement (PVM) technology - a non-invasive tool that can capture and visualize particles development in real-time. iC PVM emits a laser that illuminates the particles within the microscope probe window, and particles reflect the laser into the probe. The probe captures the reflected image through its camera. Each captured image has a known brightness and intensity, with the ratios of the former and later giving the reflectivity of the system as relative backscatter index (RBI). iC PVM software calculates the RBI, and its analysis with captured images gives the changes in the particles' shape, size, and concentration. Functional specifications of Particle view V19 are  $1300\mu\text{m} \times 890\mu\text{m} (\pm 50\mu\text{m})$  field of view,  $> 2\mu\text{m}$  optical resolution, 1500 x 1024 pixels image resolution, and eight pulsed laser diodes (4 front; 4 back) illumination. Settings used during the experiment are: front light with auto adjust, the focus was moved 100 $\mu\text{m}$  away, with sharpening and enhance features selected.

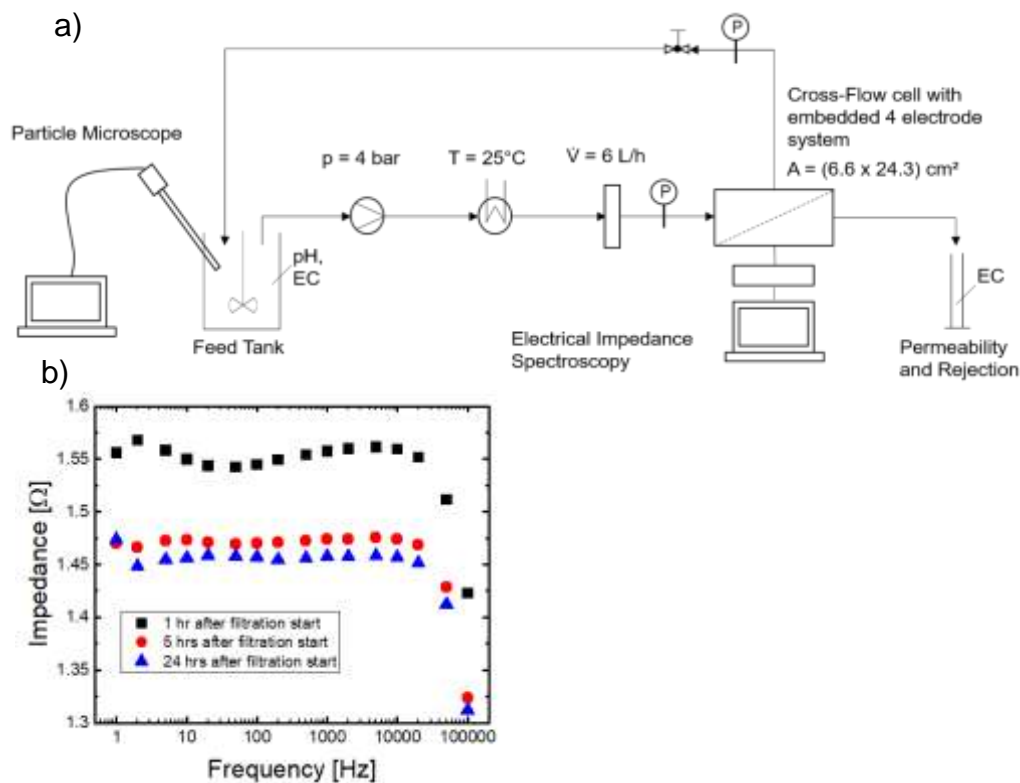


**Figure 1:** (a) Schematic of the nanofiltration experimental set-up with in-line particle microscope and in-situ electrical impedance spectroscopy, enabling real-time monitoring of mineral fouling. (b) Typical EIS scan of the entire frequency range (1 – 10<sup>5</sup> Hz), which was similar for all experiments. Data shown for CaCO<sub>3</sub> mineral scaling under low supersaturation. Weak dependence on frequency was demonstrated, with lower frequencies (1 – 10 Hz) generally being the most stable. Frequency  $\omega = 5 \text{ Hz}$  was selected.

152

153 All experiments were performed in full recirculation mode, with permeate and retentate

154 recycled into the feed tank. Concentrated synthetic wastewater effluent according to Shafdan

155 composition (Oren et al., 2007) (Table S3) was used. Experiments were performed in three

156 stages: (i.) compaction filtration using DI for 18 hours to achieve stable flux and minimize

157 sample, and reference noise of the impedance spectra; (ii.) conditioning filtration - DI water

158 was replaced with feed solution (concentrated synthetic effluent) without the scaling salt

159 components, and filtration runs for 2 hours; and (iii.) filtration experiments – started with the

160 addition of the scaling salts (Table S4) accordingly. PHREEQC was used to model similar

161 mass-based precipitation potential for both scalants in each experiment for the concentration

of added scaling salt components. Details about PHREEQC are available at S2.0. Experimental set up (Fig. 1) has a 2L feed tank stirred with a mechanical stirrer set at 200rpm throughout the experiments. The feed tank was connected via a gear pump (FluidOTech) to the INPHAZE<sup>TM</sup> filtration module, which contained the membrane. The pump was coupled with a frequency converter (EDS1000 Inverter, ENC), enabling the adjustment of the feed flow rate. Before entering the filtration module, the solution passed through a customized chiller (MRC), keeping the temperature at  $25\pm1^{\circ}\text{C}$ . Two gauges at the inlet and outlet of the module measure the transmembrane pressure (TMP). TMP at the module's outlet could be regulated by a back-pressure valve (Swagelok) from 0 to 7 bars. Additionally, retentate flow was monitored by a rotameter type flowmeter (ASV Stubbe).

The membrane sample size for crossflow-chamber of the INPHAZE<sup>TM</sup> filtration module was 243 mm x 66 mm, giving an effective membrane area of 0.016 m<sup>2</sup>. The INPHAZE<sup>TM</sup> filtration module is connected with a four electrodes system which is connected to the spectrometer unit and in turn connected to a computer. Our focus in using EIS was to investigate dynamic scaling processes occurring over relatively short timescales. Therefore, impedance measurements analysis were based on a single frequency, 5 hz (Fig. 1b), in which the dependency of impedance on frequency is weak (phase was almost zero). Therefore, at this frequency, the EIS value can be considered as pure electric resistance. The same approach was applied for membrane fouling in previous studies (Bannwarth et al., 2016; Nir et al., 2016). The pressure for all experiments was constant at  $p = 4$  bars with a feed flow rate of  $\dot{V} = 6$  L/h. The experiments were modified according to Figures S3 and S4 to study different aspects of scaling. A summary of differences in the experiments can found in Table S5. Figure S5 shows the experimental cycle used for all experiments.



### 3. Results and discussion

Following compaction and pre-conditioning stages, the filtration stage commenced with additions of 7 aliquots of  $\text{CaCO}_3$  ( $\text{CaCl}_2/\text{NaHCO}_3$ ; 8 mm each) or Ca-P ( $\text{CaCl}_2/\text{Na}_2\text{HPO}_4$ ; 6 and 4 mm each) salts respectively at 20 minutes intervals to the feed tank during 4hrs filtration run for the high supersaturation experiments. Modifications were made to the experimental procedure to investigate the different stages of fouling. Permeate flux, observed salt rejection, electrical conductivity (EC), electrical impedance spectroscopy, and in-situ online imaging (RBI and images) of crystal evolution in the feed tank were recorded in real-time during all the filtration experiments.

#### 3.1. $\text{CaCO}_3$ mineral fouling at high supersaturation

Three distinct stages in the evolution of normalized flux and electrical resistance (Fig 2a) appeared during filtration of synthetic effluent supersaturated with  $\text{CaCO}_3$ . This observation is consistent with data obtained from repeat experiments (S15), indicating the reproducibility of the experiments. In the first stage ( $t \sim 0 - 1.2$  hr), the flux decreases sharply by 25%, while at the same time, the electrical resistance of the fouling layer increased from  $\sim 0$  to  $2.5 \pm \Omega$ . In the second stage ( $t \sim 1.2 - 1.9$  hr), the flux increased by 8.0%, while the electrical resistance of the fouling layer increased moderately, reaching a peak of  $2.7 \pm \Omega$ . In the third and final stage ( $t \sim 1.9 - 4$  hr), the flux decreased moderately by 6.0% until  $t = 3.35$  hr and remained unchanged until the end of the experiment (4 hr). During that time, the electrical resistance of the fouling layer decreased slightly, reaching  $\sim 2.6 \pm \Omega$ —this complex behavior of flux and electrical resistance hints that different fouling mechanisms were in action during filtration.

208 Using real-time imaging (Fig. 2c) and light scattering (RBI) (Fig. 2b) of mineral particles in  
 209 the recycled feed solution in combination with the real-time electrical resistance and flux  
 210 measurements can underpin the dominant fouling mechanisms at each stage.

211 Our results indicate that the first stage of fouling was dominated by  $\text{CaCO}_3$  scaling, i.e.,  
 212 heterogeneous precipitation and crystallization of  $\text{CaCO}_3$  on the membrane surface (Antony  
 213 et al., 2011). The increase in fouling layer resistance is typical to scaling (Antony et al.,  
 214 2013)—the formation of a rigid crystalline layer that completely blocks water and ion

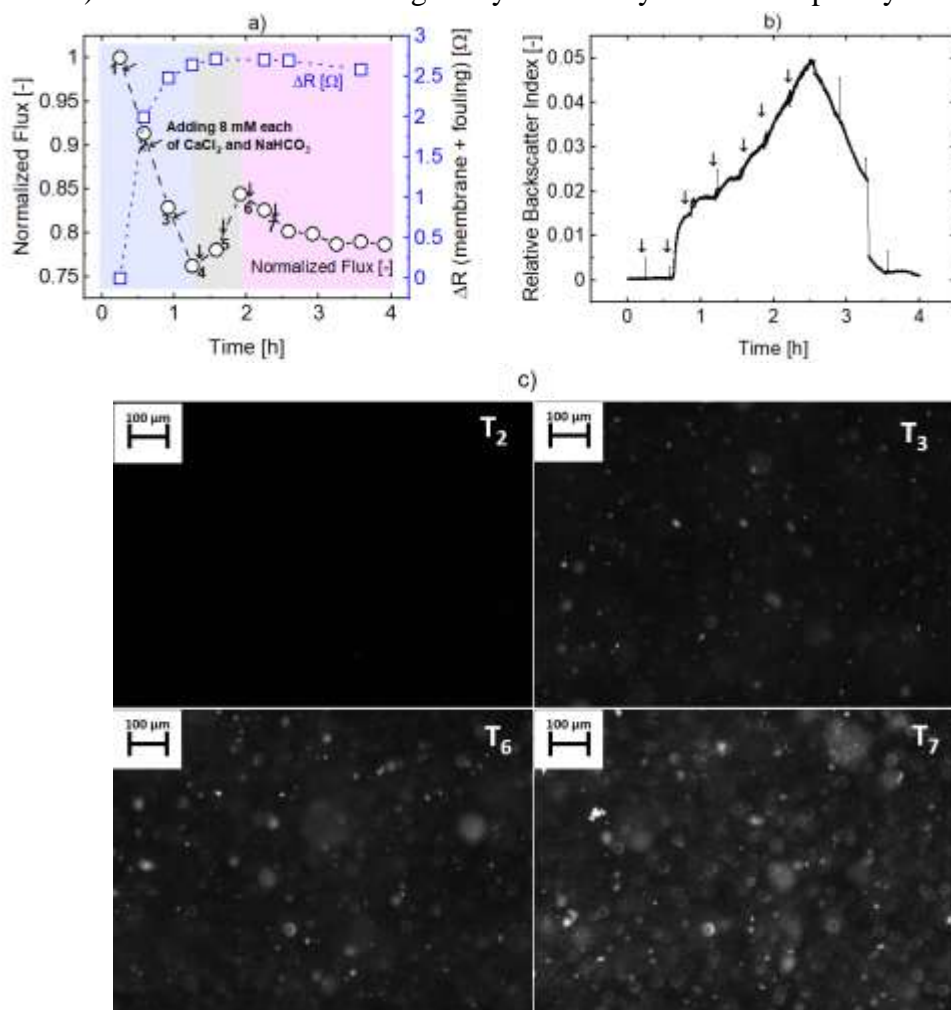


**Figure 2:** Data recorded during nanofiltration of solutions highly supersaturated with calcium carbonate (a) Normalized flux-(O) (arrows everywhere in all figures indicate the addition of scaling components, immediately after permeability measurement. The first point is the permeability of background solution without scaling salts, all permeability normalized to initial permeability) and membrane resistance-( $\square$ ) ( $\Omega$ ) (b) RBI [-] evolution, (c) and in-line real-time microscope images over the filtration time [h] for concentrated effluents NF with  $\text{CaCO}_3$ .

215 transport through the impacted membrane surface fragment. Accordingly, the RBI (Fig. 2b)

remained constant in the first 0.5 hours, and no particles were observed in the feed tank by the in-line microscope (Fig. 2c-t<sub>3</sub>). The sharp increase in RBI after 0.5 hrs is likely due to the formation of sub-micron crystal clusters (too small to be captured in images), marking the beginning of homogeneous precipitation. These tiny particles were bound to accumulate on the membrane surface and increasingly contribute to both electrical and hydraulic resistances together with the scaling layer, which was likely still the dominant mechanism at  $t \sim 0 - 1.2$  hr.

At the second stage,  $t \sim 1.2-2$  hr, the results indicated a gradual transition from mineral scaling to particulate fouling. The transition was driven by the increase of  $\text{CaCO}_3$  crystals size, as apparent from the PVM images (Fig. 2c at t<sub>3</sub> and t<sub>6</sub>). The progress of the bulk crystallization process is also indicated by the linear increase in RBI at  $\sim 1.2-2$  hr. A surprising increase in permeate flux was observed at this stage. We attribute this trend reversal to further growth of the previously ( $t \sim 0.6-1$  hr) deposited sub-micron crystals since the cake layer constructed of larger particles is more permeable and is more affected by shear-induced diffusion (Chellappah et al., 2010). The flattening of the fouling layer electric resistance curve (Fig. 2a) further supports the transition to the deposition of a cake layer comprising larger particles and consequently larger average pore size with higher ion conductance.

In the third stage,  $t \sim 2-4$  hr, our results suggest a complete shift to a particulate fouling regime. This was expressed in a milder decrease in flux with time relative to the 1<sup>st</sup> stage and a small yet distinct reduction in the electrical resistance. The latter can be attributed to cake-enhanced concentration polarisation (CECP), which was previously shown to increase the conductance of the fouling layer (Antony et al., 2013). The steady increase in RBI at  $t \sim 2-2.5$  hr (fig. 2b) and the PVM images taken at  $t \sim 2 - 2.15$  hr (Fig. 2c, t<sub>6</sub> & t<sub>7</sub>) points at further growth of  $\text{CaCO}_3$  crystals in the bulk, which resulted in the formation of a cake layer. At  $t \sim 2.5 - 4$  hr, the RBI (fig. 2b) decreased per a decrease in the particle concentration in the feed seen in the

PVM image recorded at  $t=3.25$  hr (S22). This is due to the build-up of particles on the membrane surface, as the further decrease in flux suggests. The radically different consequences to filtration performance associated with the different fouling regimes have prompted us to conduct additional experiments to differentiate between scaling and particulate fouling as described below.

## **2.2. $\text{CaCO}_3$ mineral fouling under low supersaturation**

To reinforce our findings on the signals caused by  $\text{CaCO}_3$  mineral scaling, we simulated low supersaturation in the feed to suppress bulk crystallization. This was done by extending the intervals between scaling salt additions to 1 hr or more. At  $t \sim 0 - 0.5$  hr, the normalized flux and electrical resistance (Fig 3a) development were similar to the previous experiment, as the flux decreased sharply by 9.0% and the electrical resistance of the fouling layer increased. At the same time, the RBI (Fig 3b) remained unchanged for  $t < 0.5$  hr, confirming that no particles were present in the bulk – an indication of heterogenous mineral scaling. At  $t > 0.5$  hr, the RBI increased due to the emergence of nanoparticles, too small to be captured as images by the in-line microscope. In the high supersaturation experiment, a second aliquot of scalants was added at this point, resulting in the continuation of the flux decline in the same trend. This time, however, the flux decline was flattened with the increase in RBI, which can be attributed either to fouling by nanoparticles or to a slower scaling formation due to competition with the nanoparticles' surface and lower bulk supersaturation. Accordingly, the increase in electrical resistance was flattened again, further demonstrating the high sensitivity of this method to the type of mineral fouling. At  $t=1$  hr, a second dose of scalants was added, initiating a complete transition to particulate fouling. This was indicated by the in-line

imaging (S11-T<sub>2-3</sub>), the sharp increase in RBI, the flattening in flux decline, and the moderate decrease in fouling layer electrical resistance, as in the previous set of experiments. This time, however, post-filtration SEM imaging provided additional information.

SEM images of the CaCO<sub>3</sub> crystals deposited on the membrane surface (Fig 3c) further reinforced our hypothesis regarding the dominant fouling mechanism. The deposited particles had crystalline rhombohedral sharp and straight edges – typical of calcite polymorphs (Andritsos et al., 1997), the most stable form of CaCO<sub>3</sub>. The large particles (>15 µm) appearing in the cross-sectional image (Fig 3c) and overshadowed in the bulk suspension imaging by smaller particles (S11-T<sub>2-3</sub>) suggest lateral growth on the membrane surface, affirming the assumption of heterogenous crystallization. According to the SEM images, scaling was developed as separate 'islands' that grew on the membrane and blocked the

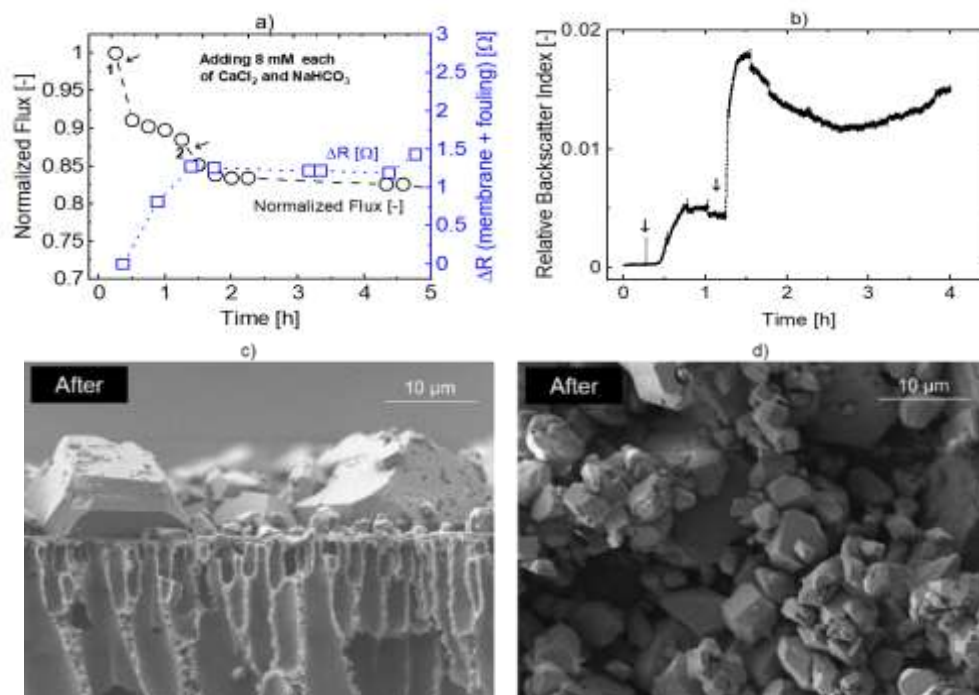


**Figure 3:** Data recorded during and after nanofiltration of solutions having low supersaturation with calcium carbonate (a) Permeability-(O) and membrane resistance-(□) [Ω] (b) RBI evolution, SEM images; (cross-sections; (c), and top view after filtration (d), with 2500x magnifications.); over the filtration time [h] for simulated low supersaturation CaCO<sub>3</sub> scaling. SEM images show crystalline particles of various sizes; large particles (>15µm) heterogeneously grew laterally on the membrane surface due to surface crystallization/scaling before homogenous crystallization. Smaller particles (<5µm) are due to homogenous crystallization. The extended graphs until 24 hr time can be found at S20.

transfer of water and ions. The smaller ( $<5\text{ }\mu\text{m}$ ) particles seen in between (Fig 3c) and on top of (Fig 3d) the larger particles corroborate our finding that particulate fouling took place after mineral scaling. The results of the particulate fouling experiment described below confirm that the smaller particles originated from bulk crystallization.

### **3.3. Particulate fouling by $\text{CaCO}_3$ crystals**

To reinforce our interpretations regarding the signals caused by particulate fouling of  $\text{CaCO}_3$  precipitates, we induced homogenous bulk crystallization in the feed tank *before* initiating filtration. This was done by adding 7 aliquots of 8 mmol ( $\text{CaCl}_2/\text{NaHCO}_3$ ) in intervals of 20 minutes, as in the high supersaturation experiments. The crystals' growth was evident from the monotonic increase in RBI (Fig. 4b) at  $t \sim 2.2 - 2.9$  hr. The sharp increase in RBI after filtration started may be due to the change in flow around the probe in the feed tank. As seen in Fig. 4a, the normalized flux increased by 4-6%, while the electrical resistance of the membrane and fouling layer decreased by  $\sim 0.8\text{ }\Omega$ . These signals are an amplified response to particulate fouling (as observed in the final fouling stage, section 3.1), i.e., negligible addition to the hydraulic resistance and cake enhanced concentration polarization. The latter is also supported by the decrease in observed salt rejection (Fig. 4c). The SEM images (Fig 4: d & e) taken after filtration show relatively homogeneous size distribution of the crystals, typical of bulk crystallization. The large crystals, indicative of their lateral growth on the membrane surface (as observed in Fig. 3c & d) are not seen in this case. The porous structure of the

fouling layer, which causes the effects described above, is clearly seen. This further affirms our interpretation of the EIS and flux signals.

### 3.4. Rapid increase of Calcium phosphate supersaturation

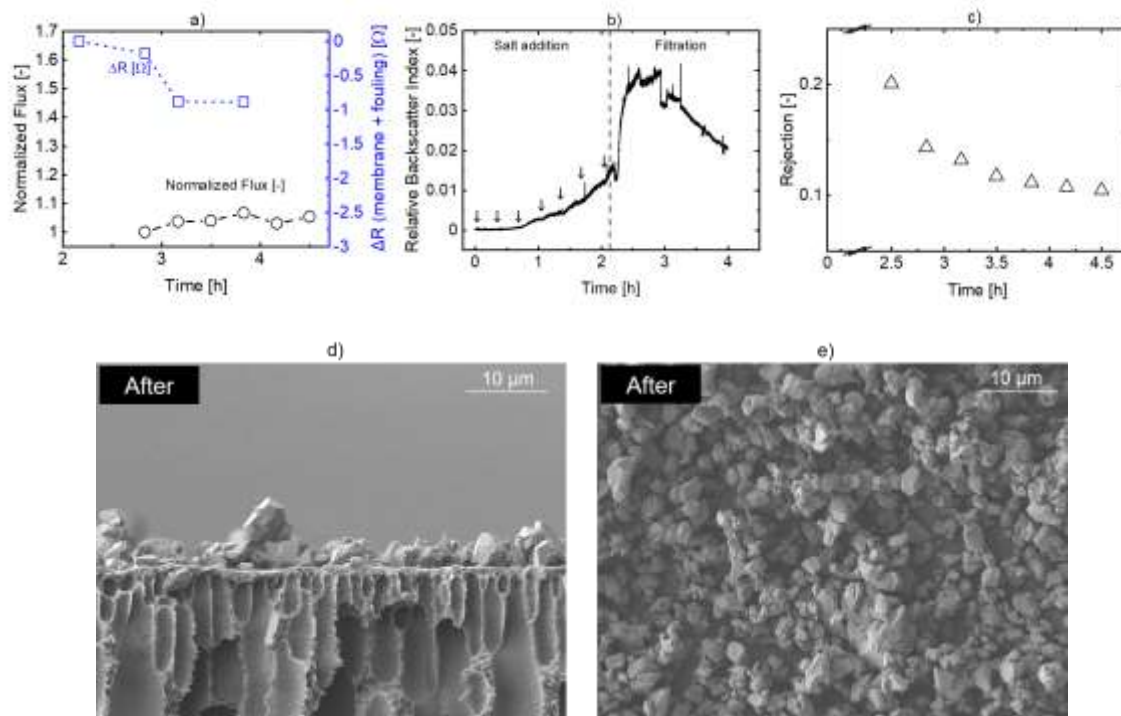


**Figure 4:** Data recorded during nanofiltration of calcium carbonate particle suspension (a) permeability-(O) and membrane resistance-(□) [Ω]; (b) RBI [-] evolution; (c) salt rejection-(Δ); SEM images (Cross Section (d), top view(e), with 2500x); over the filtration time [h] in CaCO<sub>3</sub> simulated bulk crystallization-cake filtration.

The trend of normalized flux vs. time (Fig. 5a) during filtration of synthetic effluent supersaturated with Ca-P was similar to that observed for CaCO<sub>3</sub>. Similarly, this trend is consistent with data obtained from repeat experiments (S17), indicating the reproducibility of our experiments. The trend in electrical resistance of the fouling layer was also similar; however, the time synchronization of this signal with the flux signal differs in the case of Ca-P fouling. As in CaCO<sub>3</sub> fouling, three distinct stages of flux evolution were recorded: a first stage ( $t \sim 0 - 1$  hr) in which the flux decreased sharply (43%), a second stage in which the flux increased ( $t \sim 1 - 1.25$  hr), and a third stage in which the flux decreased gradually (by

~14%). At the same time, the fouling layer electrical resistance was negligible in the first 0.5 hr (according to the absolute value shown in the Fig. S23), increased from ~0 to ~1  $\Omega$  at t ~0.5 - 1.25 hr, then increased gradually until 2.5 hr, before reaching a plateau at ~1.3  $\Omega$ . Although the trends in flux and EIS are similar between  $\text{CaCO}_3$  and  $\text{Ca-P}$ , the signals are synchronized differently in time, pointing at a different fouling mechanism.

By combining flux and EIS (Fig. 5a) with real-time microscopy (Fig. 5b & c), we were able

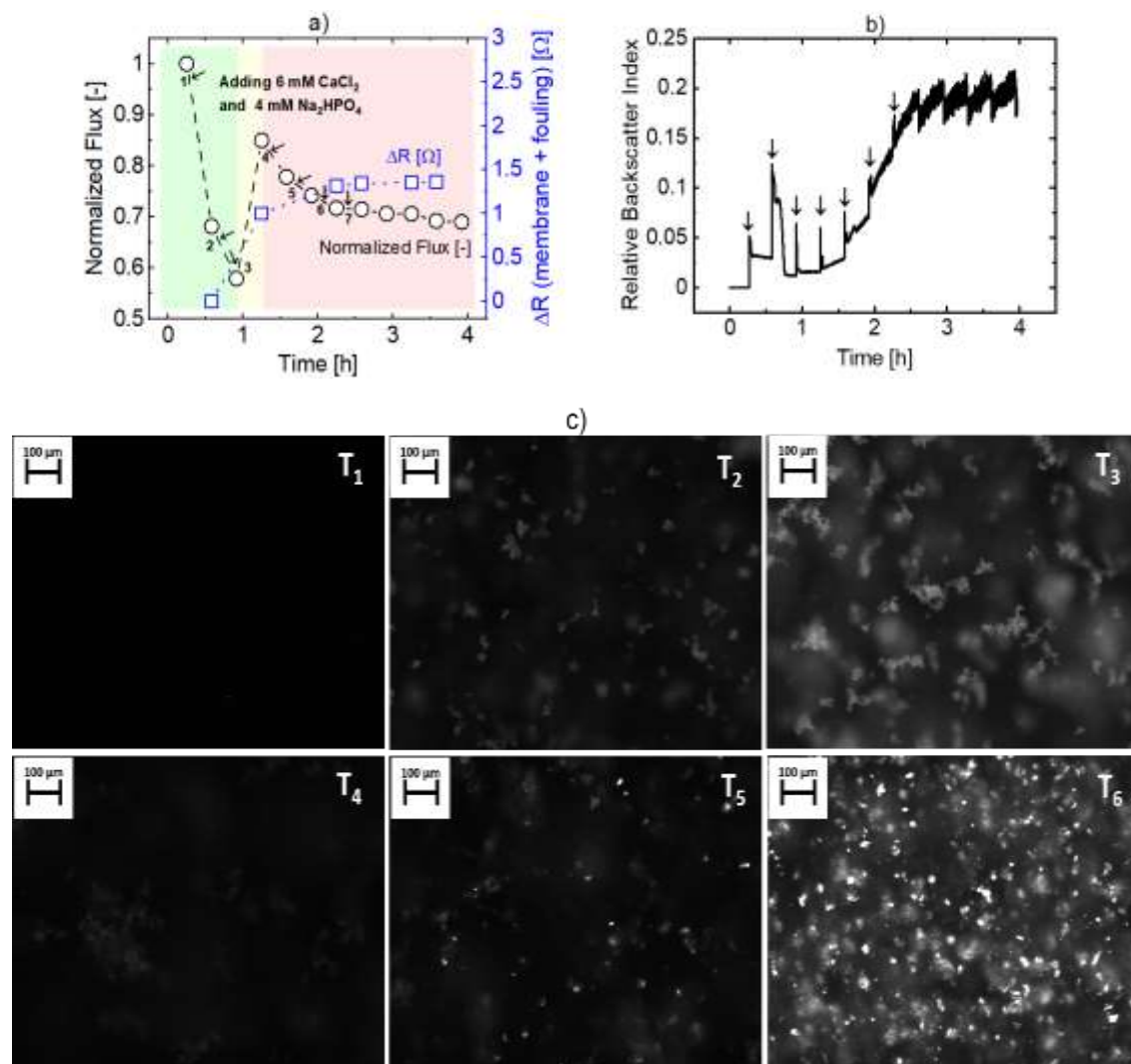


**Figure 5:** Data recorded during nanofiltration of solutions highly supersaturated with calcium phosphate (a) permeability-(O) and membrane resistance- ( $\square$ ) [ $\Omega$ ]; (b) RBI [-] evolution; (c) and in-line real-time microscope images at different time stages of filtration.

to pinpoint the mechanisms underlying membrane fouling by  $\text{Ca-P}$  minerals, as it evolved



during the nanofiltration experiment. Immediately after the first salt addition, the RBI (Fig. 5b) increased, implying that bulk precipitation already occurred at this early stage. This conclusion was supported by an independent experiment (Fig. S10), in which we found that Ca-P precipitation starts at close to zero (0.0) supersaturation of ACP and with a very short induction time (~50-100 seconds). The sharp flux decrease in this initial stage is thus attributed to the accumulation of sub-micron, highly hydrated, amorphous particles, which created a fouling layer of high hydraulic resistance. Ions, in contrast, could easily pass through this layer, indicating its porosity. After 0.5 hr (before the 2<sup>nd</sup> salt addition), the real-time imaging (Fig. 5c-t<sub>2</sub>) reveals aggregates of particles with distinct 'fluffy' morphology and low light reflectance, thus affirming bulk precipitation of amorphous particles. After the 2<sup>nd</sup> salt addition, the number of particles and size of the aggregates in the bulk further increase (Fig. 5c-t<sub>3</sub>), leading to an additional decrease in flux. Following the 3<sup>rd</sup> salt addition, the normalized flux increased from its minimum at 0.57 back to 0.85, while the electrical resistance increased sharply, indicating a change in the morphology of the layer. Indeed, the real-time particle imaging revealed a transition from amorphous precipitants (Fig. 5c, T<sub>1-3</sub>), first to a less 'flaky' and more interconnected aggregates (Fig. 5c T<sub>4</sub>), and then to a mixed-phase with crystalline components having a defined shape and high reflectance (Fig. 5c T<sub>5-6</sub>). It should be noted that the circulating feed solution is in direct contact with both the suspended particles, which were captured by the real-time imaging system and the particles in the fouling layer. Therefore, particle growth and phase transition observed in the bulk are also expected in the fouling layer, where these processes can be accelerated by concentration polarization. After this transition, the RBI increase and particle imaging indicate crystal growth in the bulk, corresponding to typical cake filtration, i.e., slow reduction in flux and negligible change in electrical resistance.

### 337 3.5. Slow increase of calcium phosphate supersaturation

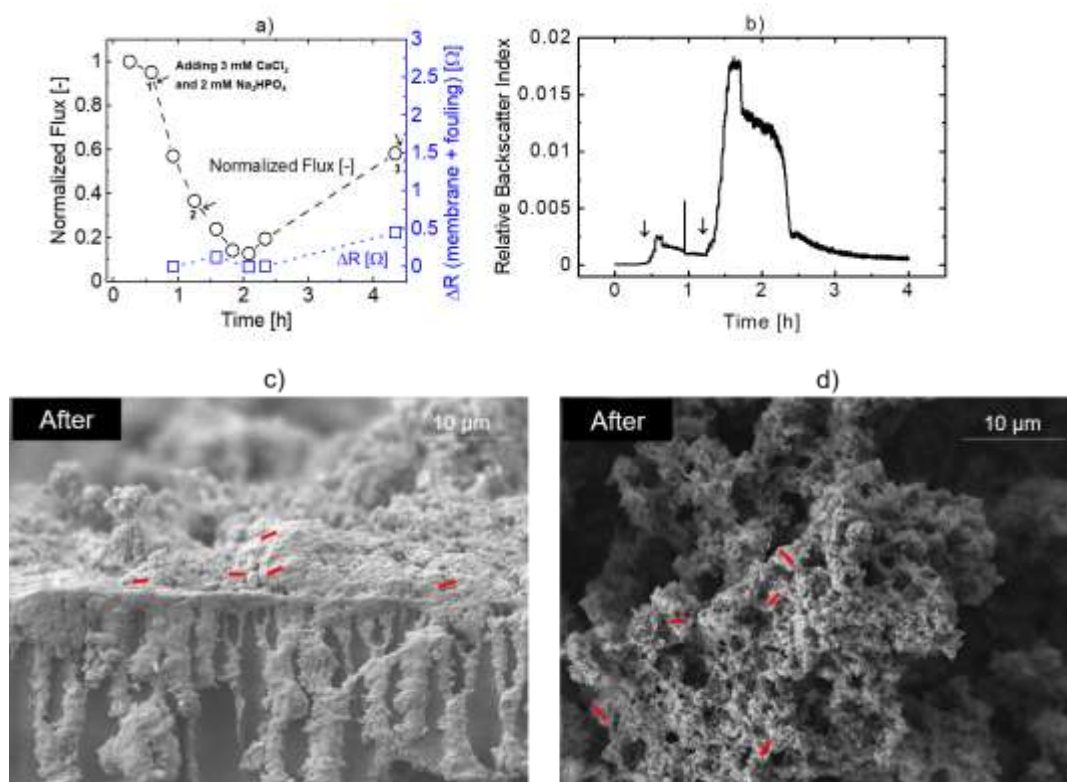


**Figure 6:** Data recorded during and after nanofiltration of solutions having low supersaturation with calcium phosphate (a) Permeability-(O) and membrane resistance-(□) [ $\Omega$ ] (b) RBI evolution, SEM images; (cross-sections; (c), and top view (d) after filtration with 2500x magnifications.); over the filtration time [h] for slow increase of Ca-P supersaturation scaling. Small red strips indicate flat surface spots. Bulk crystallization is dominant and subsequent particles deposition – forming impermeable cake layer. The extended graphs until 24 hr time can be found at S21.

To further understand the initial, low supersaturation stage of Ca-P fouling and to test our interpretation regarding the mechanism, we conducted another fouling experiment, where we increased the duration of low supersaturation. This was done by (1) adding half the amount of salt in every aliquot; (2) extending the intervals between salt aliquot to avoid fast crystallization, and; (3) splitting each aliquot to 10 equal small doses (2 min. interval) to avoid high local concentration. This procedure resulted in fouling effects similar to those described in the initial stages of the previous section, yet more 'stretched' in time, allowing us to explore this stage with better time resolution.

The results reinforce our understanding of Ca-P fouling under slow supersaturation increase and align with the results obtained for the rapid supersaturation increase (section 3.4). After

the 1<sup>st</sup> salt addition, the RBI (Fig. 6b) increased after a very short induction time, as before, then gradually decreased due to aggregation, and increased yet again after the 2<sup>nd</sup> salt addition. The RBI evolution supports the premise of Ca-P bulk precipitation as a primary fouling initiator. Due to the prolonged dominance of small particles in the circulating feed, the flux dramatically decreased by 64% and 86% after the 1<sup>st</sup> and 2<sup>nd</sup> additions, respectively, despite the lower amount of scalants added compared to the rapid supersaturation increase. This demonstrates the significant role of fouling layer morphology, influenced by the rate at which supersaturation increases. At the same time, the low and relatively constant electrical resistance value during the 1<sup>st</sup> 2.5 hrs supports the premise of a porous layer with good ion conduction and poor water conduction properties.

The results obtained at longer times (>2.5 hrs), during the slow increase of Ca-P supersaturation, further support our interpretation of the results obtained during the rapid supersaturation increase (section 3.4). Both the flux and EIS increased, showing the same trend as in section 3.4, yet after a longer time, due to lower concentrations of Ca and P. With this improved time resolution, it is visible that both the flux and EIS signals increased at the same time (Fig. 6a), reinforcing the premise of a morphological change in the fouling layer. We thus pose that dehydration and crystallization processes have condensed the layer, causing deswelling, which opened channels for faster water transport but reduced the surface available for ion transport. Condensation and dehydration of aggregates were previously recorded during the aging of amorphous Ca-P (Xie et al., 2014). Evidence for a phase transition can also be seen in the SEM images taken post-filtration. In both cross-sectional (Fig. 6c) and top view (Fig. 6d), flat surfaces (indicated by small red strips) of higher crystallinity can be spotted within the dense semi-porous fouling layer. Precipitant seen below the membrane surface is probably minerals that were smeared on the cross-section when cutting the membrane in preparation for SEM imaging. Intra-pore fouling is not likely

because the rejection of hydrogen phosphate by this membrane is very high (>90% see independent experiment in S24). In this stage, the drop in RBI indicates aggregation of small particles, which is a precursor for Ca-P phase transformation and crystal growth (Čadež et al., 2018; Xie et al., 2014).

### **3.6. Particulate fouling by Ca-P crystals**

To isolate the effect of fouling by the more crystalline Ca-P phase, we induced bulk precipitation in the feed tank by adding 7 aliquots of scaling salts ( $\text{CaCl}_2/\text{Na}_2\text{HPO}_4$ , 6 and 4 mmol, respectively), at 20 minutes interval prior to the filtration step. After the first two additions, the RBI signal (Fig. 7b) sharply increased due to the rapid formation of small particles. After the third addition, the RBI decreased due to aggregation followed by crystallization, as was also captured by the in-line imaging system (S14-T<sub>3</sub>). The RBI remained low until filtration started (apart from local spikes on salt additions), indicating that no secondary nucleation has occurred. The RBI increased with the beginning of filtration (and the end of salt additions), likely due to shear forces causing the aggregates to break. As expected in fouling by large particles, the flux and electrical resistance (Fig. 7a) (9% and  $\Delta R = -0.25 \Omega$  respectively) slightly decreased (9%). The decrease in salt rejection (Fig. 7c) further supported the occurrence of CECP. Overall, the trends in RBI, flux, and electrical resistance recorded during this induced fouling by Ca-P matches our interpretation of the final stage during the rapid increase of Ca-P supersaturation (section 3.4).

The SEM images (Fig. 7d&e) reveal the morphology of the Ca-P precipitants and the fouling layer they have formed on the membrane surface. A mixed layer is seen, containing

amorphous-looking aggregates, together with mature crystal platelets. The cross-sectional image (Fig 7d) reveals significant variations in the layer thickness that can be attributed to its heterogeneity. This heterogeneity is visible in the top-view image (Fig. 7e), also showing the contrast between the two phases. Compared to the fouling layer seen after the slow increase in Ca-P supersaturation (Fig. 6c), the amorphous phase is similar but seems less dense and more porous. It also appears that the deposited crystals disturbed the formation of a continuous dense layer, which again highlights the importance of morphology in mineral fouling.

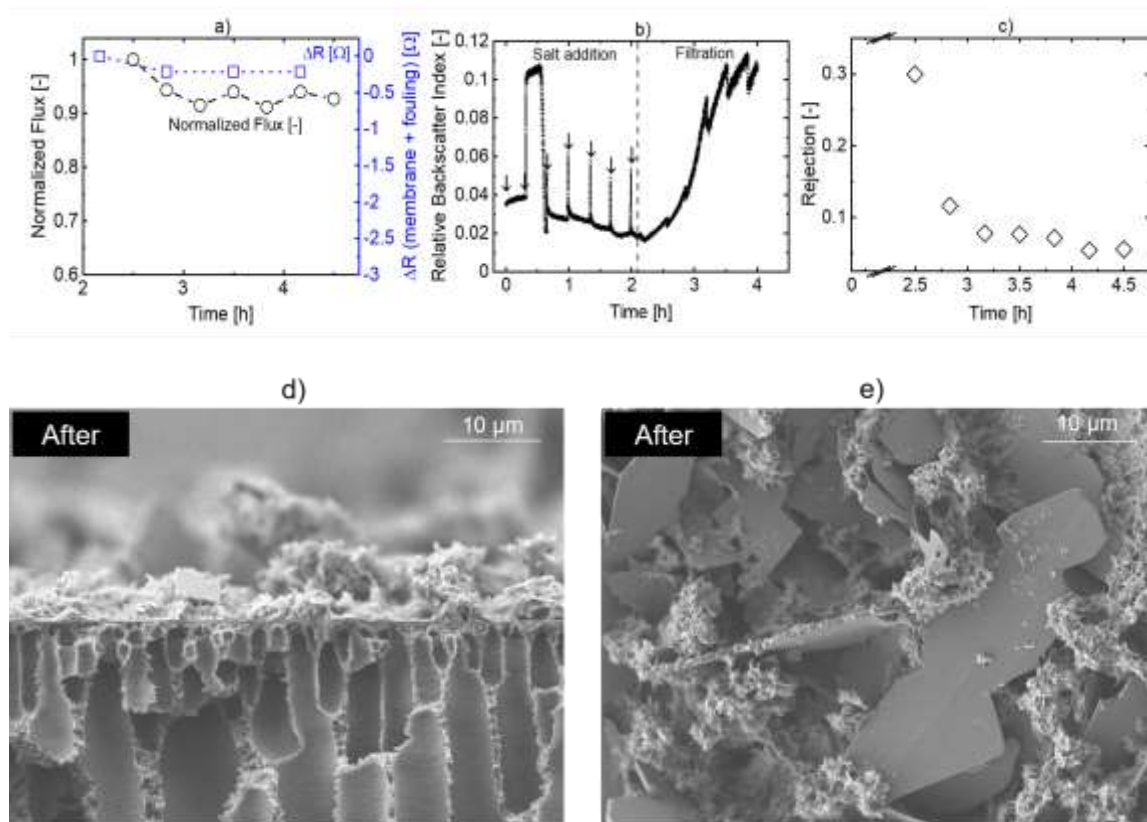


**Figure 7:** Data recorded during nanofiltration of calcium phosphate particle suspension (a) permeability-(O) and membrane resistance-(□) [Ω]; (b) RBI [-] evolution; (c) salt rejection-(◇); SEM images (Cross Section (d), top view(e), with 2500x); over the filtration time [h] in Ca-P simulated bulk crystallization-cake filtration.

#### 4. Summary and Conclusions

406 In this work, we studied membrane fouling by  $\text{CaCO}_3$  and Ca-P minerals, using a novel  
407 combination of real-time probing techniques: in-line particle imaging and EIS. This  
408 combination was found highly useful, enabling us to uncover scaling mechanisms and  
409 distinguish between them. Using these methods to study fouling by other minerals, such as  
410 silica or iron oxides, will likely result in further insights. Complementary data gathered from  
411 iC PVM, EIS, flux measurement, and post-filtration SEM imaging was used to reconstruct  
412 how morphological changes induced by, e.g., aggregation, particle growth, and  
413 crystallization determine the development of mineral fouling and its impact on filtration. The  
414 morphological changes were found to depend on the mineral type, filtration time, and rate of  
415 supersaturation increase.

416 For  $\text{CaCO}_3$  (Fig. 8a), the results imply that upon the increase in supersaturation,  
417 heterogeneous precipitation on the membrane surface began, forming impermeable scaling  
418 'islands' on the membrane surface. Consequently, the surface available to the transport of  
419 both water and ions decreased. Upon further increase in supersaturation, the crystalline  
420 scaling islands grew towards the sides and the top, further reducing flux and ion conductance.  
421 At the same time, sub-micron particles started to form via bulk precipitation. Deposition of  
422 these small particles between the scaling islands decreased the water flux but had a negligible  
423 effect on ion passage. With further supersaturation increase and longer filtration time, the  
424 surface area of the suspended particles gradually increased (with their size and number) until  
425 it overshadowed the surface area of the scaling islands. This marked a transition from a  
426 scaling regime to a particulate fouling regime. At the same time, the particles in the fouling  
427 layer also grew (some possibly sheared of the membrane surface), thus enabling faster water  
428 transport and partial recovery of the water flux. With further increase in supersaturation,  
429 larger particles formed in the bulk deposited on and between the scaling islands, slightly

hindering water transport but increasing electrical conductivity in the fouling layer due to  
cake enhanced concentration polarization of ions.

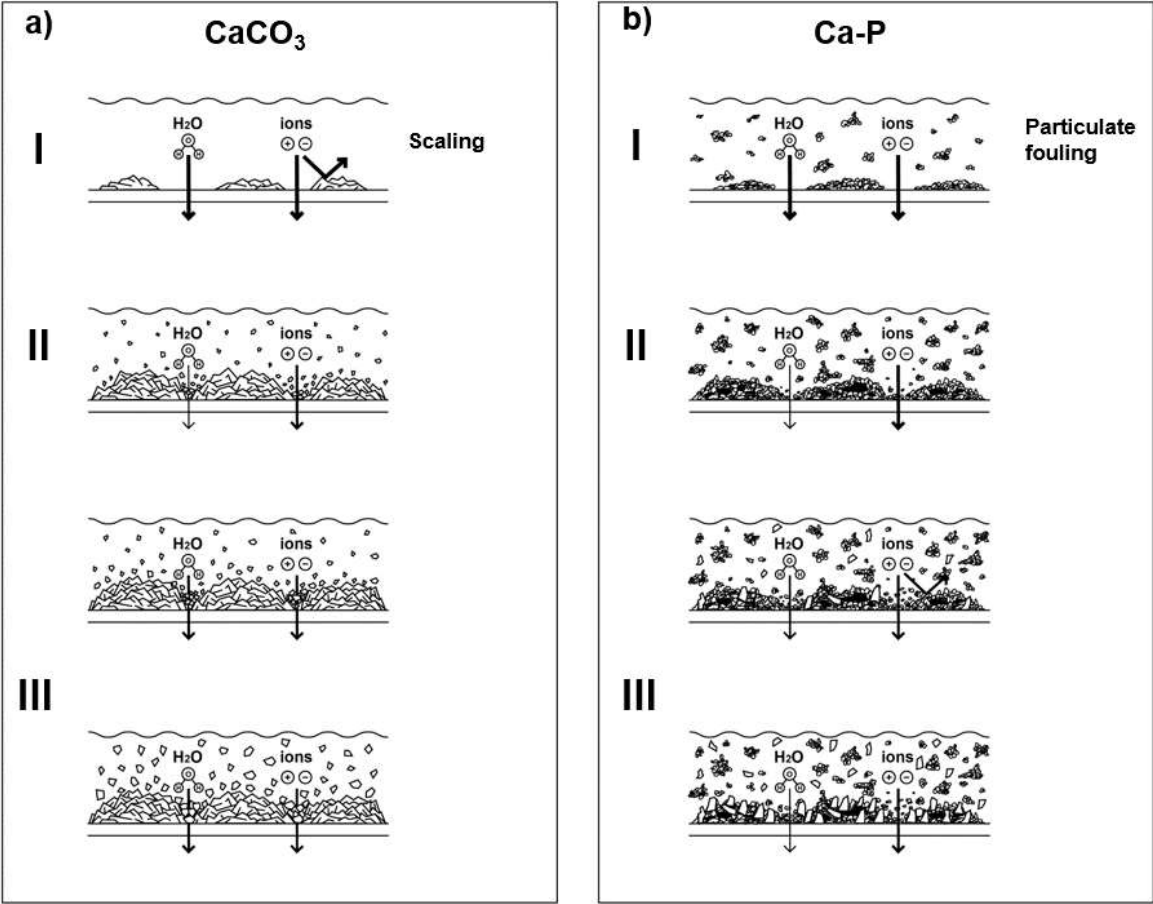


**Figure 8:** Illustration of the proposed mechanism of mineral fouling evolution with time based on the real-time monitoring and post-filtration microscopy (a) CaCO<sub>3</sub> scaling evolution stages initiated with scaling/surface crystallization and transforms to particulate fouling; (b) Ca-P fouling evolution stages, initially with amorphous particulates and transforms into crystalline particulates.

For Ca-P (Fig.8b), the results imply that mineral fouling is initiated by bulk precipitation, occurring at very low supersaturation with almost no induction time. At the conditions studied, the precipitant is initially composed of amorphous, highly hydrated sub-micron particles, which deposit on the membrane. Consequently, a porous fouling layer is formed, hindering water transport but allowing ions to pass through. With the increase in supersaturation and at longer filtration time, the smaller particles aggregated, followed by

dehydration and consolidation of the amorphous Ca-P, as part of its aging process. Some of the aggregates may have detached from the surface by sheer force. This resulted in a dense layer with holes and cracks, allowing faster ion passage but hindering water transport. After a further increase in supersaturation and filtration time, the phase transition progresses, and plate-shaped crystals appear. These crystals deposit and accumulate on the membrane, forming a top cake layer that inhibits water transport, but increased electrical conductivity through cake enhanced concentration polarization of ions.

Our findings have practical implications for the control and mitigation of mineral fouling, which is essential for obtaining a high recovery in wastewater effluent nanofiltration and reverse osmosis. We show evidence that under typical effluent filtration conditions, ACP formed in the retentate solution controls the initial stages of Ca-P fouling. Therefore, modifying the membrane surface is not expected to contribute to scaling mitigation significantly. We also observed that ACP starts precipitating at a very low supersaturation level and with practically no induction time, making the saturation index a practical scaling control parameter. In contrast,  $\text{CaCO}_3$  fouling is initially controlled by surface scaling, which starts after a significantly shorter induction time compared to bulk precipitation. Compared to  $\text{CaCO}_3$  scaling, Ca-P fouling is more reversible and could be more easily controlled by crossflow cleaning or backwash. Acid cleaning should also be more effective for a porous layer (as compared to the crystalline scaling layer) since the liquid-solid contact area is higher. Thus,  $\text{CaCO}_3$  scaling should be avoided. We found that when the retained solution contains larger and more crystalline mineral particles, the effect of fouling on filtration performance is less severe. This raises interesting possibilities to control mineral fouling by introducing seeds at an intermediate filtration stage. In our future work, we plan to implement and test this novel strategy.



## Acknowledgments

This work was funded by the Ministry of Science and Technology (MOST) Israel, under the framework of German-Israeli Water Technology Research (Project: 8764961). We also thank the Young Scientists Exchange Program (YSEP) of the BMBF-MOST Cooperation in Water Technology Research.

## References

- Almuktar, S.A.A.A.N., Abed, S.N., Scholz, M., 2018. Wetlands for wastewater treatment and subsequent recycling of treated effluent: a review. *Environ. Sci. Pollut. Res.* <https://doi.org/10.1007/s11356-018-2629-3>
- Andritsos, N., Karabelas, A.J., Koutsoukos, P.G., 1997. Morphology and structure of  $\text{CaCO}_3$  scale layers formed under isothermal flow conditions. *Langmuir*. <https://doi.org/10.1021/la960960s>
- Antony, A., Chilcott, T., Coster, H., Leslie, G., 2013. In situ structural and functional characterization of reverse osmosis membranes using electrical impedance spectroscopy. *J. Memb. Sci.* <https://doi.org/10.1016/j.memsci.2012.09.028>
- Antony, A., How, J., Gray, S., Childress, A.E., Le-clech, P., Leslie, G., 2011. Scale formation and control in high pressure membrane water treatment systems : A review. *J. Memb. Sci.* 383, 1–16. <https://doi.org/10.1016/j.memsci.2011.08.054>
- Bannwarth, S., Trieu, T., Oberschelp, C., Wessling, M., 2016. On-line monitoring of cake layer structure during fouling on porous membranes by in situ electrical impedance analysis. *J. Memb. Sci.* <https://doi.org/10.1016/j.memsci.2016.01.009>
- Bunani, S., Yörükoğlu, E., Sert, G., Yüksel, Ü., Yüksel, M., Kabay, N., 2013. Application

487 of nanofiltration for reuse of municipal wastewater and quality analysis of product  
 488 water. *Desalination* 315, 33–36. <https://doi.org/10.1016/J.DESAL.2012.11.015>

489 Čadež, V., Erceg, I., Selmani, A., Domazet Jurašin, D., Šegota, S., Lyons, D., Kralj, D.,  
 490 Sikirić, M., 2018. Amorphous Calcium Phosphate Formation and Aggregation Process  
 491 Revealed by Light Scattering Techniques. *Crystals* 8, 254.  
 492 <https://doi.org/10.3390/cryst8060254>

493 Chang, I.S., Lee, S.S., Choe, E.K., 2009. Digital textile printing (DTP) wastewater  
 494 treatment using ozone and membrane filtration. *Desalination*.  
 495 <https://doi.org/10.1016/j.desal.2008.01.014>

496 Chaussemier, M., Pourmohtasham, E., Gelus, D., Pécou, N., Perrot, H., Lédion, J., Cheap-  
 497 Charpentier, H., Horner, O., 2015. State of art of natural inhibitors of calcium  
 498 carbonate scaling. A review article. *Desalination*.  
 499 <https://doi.org/10.1016/j.desal.2014.10.014>

500 Chellappah, K., Tarleton, S., Wakeman, R., 2010. The porosity, permeability and  
 501 restructuring of heterogeneous filter cakes. *Chem. Eng. Technol.*  
 502 <https://doi.org/10.1002/ceat.201000093>

503 Chen, T., Neville, A., Yuan, M., 2006. Influence of  $Mg^{2+}$  on  $CaCO_3$  formation-bulk  
 504 precipitation and surface deposition. *Chem. Eng. Sci.*  
 505 <https://doi.org/10.1016/j.ces.2006.04.007>

506 Farhadkhani, M., Nikaeen, M., Yadegarfar, G., Hatamzadeh, M., Pourmohammadbagher,  
 507 H., Sahbaei, Z., Rahmani, H.R., 2018. Effects of irrigation with secondary treated  
 508 wastewater on physicochemical and microbial properties of soil and produce safety in  
 509 a semi-arid area. *Water Res.* <https://doi.org/10.1016/j.watres.2018.07.047>

510 Friedler, E., 2001. Water reuse - An integral part of water resources management: Israel as  
511 a case study. *Water Policy*. [https://doi.org/10.1016/S1366-7017\(01\)00003-4](https://doi.org/10.1016/S1366-7017(01)00003-4)

512 Garcia, X., Pargament, D., 2015. Reusing wastewater to cope with water scarcity:  
513 Economic, social and environmental considerations for decision-making. *Resour.*  
514 *Conserv. Recycl.* <https://doi.org/10.1016/j.resconrec.2015.05.015>

515 Gilron, J., Hasson, D., 1987. Calcium sulphate fouling of reverse osmosis membranes: Flux  
516 decline mechanism. *Chem. Eng. Sci.* [https://doi.org/10.1016/0009-2509\(87\)80109-4](https://doi.org/10.1016/0009-2509(87)80109-4)

517 Grandclément, C., Seyssiecq, I., Piram, A., Wong-Wah-Chung, P., Vanot, G., Tiliacos, N.,  
518 Roche, N., Doumenq, P., 2017. From the conventional biological wastewater treatment  
519 to hybrid processes, the evaluation of organic micropollutant removal: A review.  
520 *Water Res.* 111, 297–317. <https://doi.org/10.1016/J.WATRES.2017.01.005>

521 Greenberg, G., Hasson, D., Semiat, R., 2005. Limits of RO recovery imposed by calcium  
522 phosphate precipitation. *Desalination*. <https://doi.org/10.1016/j.desal.2005.04.026>

523 Greenlee, L.F., Testa, F., Lawler, D.F., Freeman, B.D., Moulin, P., 2010. The effect of  
524 antiscalant addition on calcium carbonate precipitation for a simplified synthetic  
525 brackish water reverse osmosis concentrate. *Water Res.*  
526 <https://doi.org/10.1016/j.watres.2010.02.024>

527 Kaganovich, M., Zhang, W., Freger, V., Bernstein, R., 2019. Effect of the membrane  
528 exclusion mechanism on phosphate scaling during synthetic effluent desalination.  
529 *Water Res.* <https://doi.org/10.1016/j.watres.2019.06.013>

530 Kappel, C., Kemperman, A.J.B., Temmink, H., Zwijnenburg, A., Rijnaarts, H.H.M.,  
531 Nijmeijer, K., 2014. Impacts of NF concentrate recirculation on membrane  
532 performance in an integrated MBR and NF membrane process for wastewater

533 treatment. J. Memb. Sci. <https://doi.org/10.1016/j.memsci.2013.11.023>

534 Klepetsanis, P.G., Koutsoukos, P.G., 1989. Precipitation of calcium sulfate dihydrate at  
 535 constant calcium activity. J. Cryst. Growth. [https://doi.org/10.1016/0022-](https://doi.org/10.1016/0022-0248(89)90164-4)  
 536 0248(89)90164-4

537 Lee, S., Lee, C.-H., 2005. Scale formation in NF/RO: Mechanism and control, Water  
 538 Science and Technology.

539 Lee, S., Lee, C.H., 2000. Effect of operating conditions on CaSO<sub>4</sub> scale formation  
 540 mechanism in nanofiltration for water softening. Water Res.  
 541 [https://doi.org/10.1016/S0043-1354\(00\)00142-1](https://doi.org/10.1016/S0043-1354(00)00142-1)

542 Luo, Y., Guo, W., Hao, H., Duc, L., Ibney, F., Zhang, J., Liang, S., Wang, X.C., Ngo, H.H.,  
 543 Nghiem, L.D., Hai, F.I., Zhang, J., Liang, S., Wang, X.C., 2014. A review on the  
 544 occurrence of micropollutants in the aquatic environment and their fate and removal  
 545 during wastewater treatment. Sci. Total Environ. 473–474, 619–641.  
 546 <https://doi.org/10.1016/j.scitotenv.2013.12.065>

547 Mangal, M.N., Salinas-Rodriguez, S.G., Dusseldorp, J., Kemperman, A.J.B., Schippers,  
 548 J.C., Kennedy, M.D., van der Meer, W.G.J., 2021. Effectiveness of antiscalants in  
 549 preventing calcium phosphate scaling in reverse osmosis applications. J. Memb. Sci.  
 550 623, 119090. <https://doi.org/10.1016/j.memsci.2021.119090>

551 Mohammad, A.W., Teow, Y.H., Ang, W.L., Chung, Y.T., Oatley-Radcliffe, D.L., Hilal, N.,  
 552 2015. Nanofiltration membranes review: Recent advances and future prospects.  
 553 Desalination 356, 226–254. <https://doi.org/10.1016/J.DESAL.2014.10.043>

554 Murgolo, S., Franz, S., Arab, H., Bestetti, M., Falletta, E., Mascolo, G., 2019. Degradation  
 555 of emerging organic pollutants in wastewater effluents by electrochemical

556 photocatalysis on nanostructured TiO<sub>2</sub> meshes. Water Res.

557 <https://doi.org/10.1016/j.watres.2019.114920>

558 Nghiem, L.D., Fujioka, T., 2016. Removal of Emerging Contaminants for Water Reuse by

559 Membrane Technology, in: Emerging Membrane Technology for Sustainable Water

560 Treatment. <https://doi.org/10.1016/B978-0-444-63312-5.00009-7>

561 Nir, O., Sengpiel, R., Wessling, M., 2018. Closing the cycle: Phosphorus removal and

562 recovery from diluted effluents using acid resistive membranes. Chem. Eng. J. 346,

563 640–648. <https://doi.org/10.1016/j.cej.2018.03.181>

564 Nir, O., Trieu, T., Bannwarth, S., Wessling, M., 2016. Microfiltration of deformable

565 microgels. Soft Matter 12, 6512–6517. <https://doi.org/10.1039/c6sm01345g>

566 Oren, O., Gavrieli, I., Burg, A., Guttman, J., Lazar, B., 2007. Manganese mobilization and

567 enrichment during soil aquifer treatment (SAT) of effluents, the Dan Region Sewage

568 Reclamation Project (Shafdan), Israel. Environ. Sci. Technol. 41, 766–772.

569 <https://doi.org/10.1021/es060576+>

570 Oron, G., Gillerman, L., Buriakovsky, N., Bick, A., Gargir, M., Dolan, Y., Manor, Y., Katz,

571 L., Hagin, J., 2008. Membrane technology for advanced wastewater reclamation for

572 sustainable agriculture production. Desalination 218, 170–180.

573 <https://doi.org/10.1016/J.DESAL.2006.09.033>

574 Rathinam, K., Oren, Y., Petry, W., Schwahn, D., Kasher, R., 2018. Calcium phosphate

575 scaling during wastewater desalination on oligoamide surfaces mimicking reverse

576 osmosis and nanofiltration membranes. Water Res.

577 <https://doi.org/10.1016/j.watres.2017.10.055>

578 Roques, H., Girou, A., 1974. Kinetics of the formation conditions of carbonate tartars.

579 Water Res. [https://doi.org/10.1016/0043-1354\(74\)90105-5](https://doi.org/10.1016/0043-1354(74)90105-5)

580 Schäfer, A.I., Fane, A.G., Waite, T.D., 1998. Nanofiltration of natural organic matter:  
 581 Removal, fouling and the influence of multivalent ions. *Desalination* 118, 109–122.  
 582 [https://doi.org/10.1016/S0011-9164\(98\)00104-0](https://doi.org/10.1016/S0011-9164(98)00104-0)

583 Steiner, Z., Rapaport, H., Oren, Y., Kasher, R., 2010. Effect of surface-exposed chemical  
 584 groups on calcium-phosphate mineralization in water-treatment systems. *Environ. Sci.*  
 585 *Technol.* <https://doi.org/10.1021/es101773t>

586 Tong, T., Wallace, A.F., Zhao, S., Wang, Z., 2019. Mineral scaling in membrane  
 587 desalination: Mechanisms, mitigation strategies, and feasibility of scaling-resistant  
 588 membranes. *J. Memb. Sci.* <https://doi.org/10.1016/j.memsci.2019.02.049>

589 Tran, Q.K., Schwabe, K.A., Jassby, D., 2016. Wastewater reuse for agriculture:  
 590 Development of a regional water reuse decision-support model (RWRM) for cost-  
 591 effective irrigation sources. *Environ. Sci. Technol.*  
 592 <https://doi.org/10.1021/acs.est.6b02073>

593 Tzotzi, C., Pahiadaki, T., Yiantisios, S.G., Karabelas, A.J., Andritsos, N., 2007. A study of  
 594 CaCO<sub>3</sub> scale formation and inhibition in RO and NF membrane processes. *J. Memb.*  
 595 *Sci.* <https://doi.org/10.1016/j.memsci.2007.03.031>

596 Van De Lisdonk, C.A.C., Van Paassen, J.A.M., Schippers, J.C., 2000. Monitoring scaling  
 597 in nanofiltration and reverse osmosis membrane systems. *Desalination*.  
 598 [https://doi.org/10.1016/S0011-9164\(00\)00139-9](https://doi.org/10.1016/S0011-9164(00)00139-9)

599 Voutchkov, N., 2011. Overview of seawater concentrate disposal alternatives. *Desalination*  
 600 273, 205–219. <https://doi.org/10.1016/J.DESAL.2010.10.018>

601 Wintgens, T., Melin, T., Schäfer, A., Khan, S., Muston, M., Bixio, D., Thoeye, C., 2005.

The role of membrane processes in municipal wastewater reclamation and reuse.

Desalination. <https://doi.org/10.1016/j.desal.2004.12.014>

Xie, B., Halter, T.J., Borah, B.M., Nancollas, G.H., 2014. Tracking amorphous precursor formation and transformation during induction stages of nucleation. Cryst. Growth Des. 14, 1659–1665. <https://doi.org/10.1021/cg401777x>

Xu, P., Bellona, C., Drewes, J.E., 2010. Fouling of nanofiltration and reverse osmosis membranes during municipal wastewater reclamation: Membrane autopsy results from pilot-scale investigations. J. Memb. Sci. <https://doi.org/10.1016/j.memsci.2010.02.037>

## Graphical Abstract

